23

Photonic Realization of Qudit Quantum Computing

Yuchen Wang, Zixuan Hu, and Sabre Kais

Department of Chemistry, Department of Physics and Purdue Quantum Science and Engineering Institute, Purdue University, 560 Oval Dr, West Lafayette, IN 47907, USA

23.1 Introduction to Qudit Quantum Computing

Qudit is an alternative to qubit as the basic computational element for a quantum computer. A *qudit* is a quantum version of d-ary digits whose state can be described by a vector in the d dimensional Hilbert space $\mathscr{H}_d$ [1]. A set of orthonormal basis vectors $\{|0\rangle, |1\rangle, |2\rangle, \ldots, |d-1\rangle\}$ is used to span this space. A general form of the qudit state is

$$|\alpha\rangle = \alpha_0 |0\rangle + \alpha_1 |1\rangle + \alpha_2 |2\rangle + \cdots + \alpha_{d-1} |d-1\rangle = \begin{pmatrix} \alpha_0 \\ \alpha_1 \\ \alpha_2 \\ \vdots \\ \alpha_{d-1} \end{pmatrix} \in \mathbb{C}^d \tag{23.1}$$

where $|\alpha_0|^2 + |\alpha_1|^2 + |\alpha_2|^2 + \cdots + |\alpha_{d-1}|^2 = 1$. This section introduces the basic knowledge and concepts of the qudit quantum computing that includes qudit gates and universality in Section 23.1.1 and the important qudit algorithms such as quantum Fourier transform (QFT) and Phase Estimation Algorithm (PEA) in Section 23.1.2. The qudit system, with a state space larger than that of a qubit to store and process information, can reduce the circuit complexity, simplify the experimental setup, and enhance the algorithm efficiency [2].

23.1.1 Universality and Examples of Qudit Gates

Qudit gates are used to alter the state of a qudit and thus perform the computational operations. In quantum computation, the universal quantum gate set is defined as a set of matrices $U_k \in U(d^n)$ such that any arbitrary unitary transformation U of the Hilbert space $\mathscr{H}_d^{\otimes n}$ can be approximated via the product of its elements within the tolerance of error [3]. The idea of *universality* can be applied to the qudit logic [4–9] and there are several proposals and discussions of the standards for a universal qudit

Photonic Quantum Technologies: Science and Applications, First Edition. Edited by Mohamed Benyoucef.

gate set. In order to precisely simulate any unitary $U \in U(d^n)$ and thus set the criteria for the exact qudit universality, Vlasov shows that two noncommuting single qudit gates and a two-qudit gate are enough [3], while Brylinski and Brylinski show that a two-qudit gate with entangled qudits combined with some random single qudit gates are enough [1]. With these recipes any qudit gates can be reduced to sequences of elementary qudit gates of lower-dimension [10, 11]. Muthukrishnan and Stroud provide a physically workable procedure for building a universal qudit gate set, which implements the spectral decomposition of unitary transformations and involves a gate library of continuous parameter gates [12]. Luo and Wang propose a modified set comprising one-qudit general rotation gates and two-qudit controlled extensions of rotation gates that has gained a reduction in the gate requirement [13]. Brennen et al. provide a universal gate library with a fixed set of one qudit operations and a single free parameter "controlled phase" gate that utilize the QR decomposition of unitary transformations [14].

Many of the qubit gate either has a qudit variant or can be generalized to d dimension. For examples, the d dimension Pauli Z gate and Pauli X gate are in the matrix forms given by: [15–18]

$$X_d = \begin{pmatrix} 0 & 0 & \cdots & 0 & 1 \\ 1 & 0 & \cdots & 0 & 0 \\ 0 & 1 & \cdots & 0 & 0 \\ \vdots & \vdots & \ddots & \vdots & \vdots \\ 0 & 0 & \cdots & 1 & 0 \end{pmatrix}, \quad Z_d = \begin{pmatrix} 1 & 0 & 0 & \cdots & 0 \\ 0 & \omega & 0 & \cdots & 0 \\ 0 & 0 & \omega^2 & \cdots & 0 \\ \vdots & \vdots & \vdots & \ddots & 0 \\ 0 & 0 & 0 & \cdots & \omega^{d-1} \end{pmatrix} \tag{23.2}$$

in which ω is the dth root of unity. Other gates such as the qudit version of $\pi/8$ gate [19], SWAP gate [20–27], Toffoli gate [28, 29] have been proposed and reviewed in Ref. [2]. From the discussion of qudit universality, we know that the two-qudit gate, such as a qudit-controlled gate, is an indispensable component for universality. Since qudits have multiple states to be utilized, a qudit-controlled gate can accomplish operations of greater complexity than its qubit counterpart [30]. To fully utilize the d states on the control qudit, we discuss the *multi-value-controlled gate* (*MVCG*) for qudits. The *MVCG* can assign a unique operation to the target qudit for each corresponding state of the control qudit in one shot and within a single controlled-gate [31]. For a d-dimensional qudit system, the mathematical form of a two-qudit MVCG is a $d^2 \times d^2$ matrix given by:

$$\text{MVCG} = \begin{pmatrix} U_0 & 0 & 0 & \cdots & 0 \\ 0 & U_1 & 0 & \cdots & 0 \\ 0 & 0 & U_2 & \cdots & 0 \\ \vdots & \vdots & \vdots & \ddots & 0 \\ 0 & 0 & 0 & \cdots & U_{d-1} \end{pmatrix} \tag{23.3}$$

where each U_i $(i = 0, 1, \ldots, d-1)$ can be any given single-qudit unitary operation. The U_i operation is applied to the target qudit when the control qudit is in the $|i\rangle$ state. In Section 23.2.1, we show how to implement *MVCG* on a photonic system and how the *MVCG* can improve the efficiency of the circuit by reducing the gate requirement.

23.1.2 Examples of Qudit Quantum Algorithms

The quantum Fourier transform algorithm is the key component of many quantum algorithms [32]. It can be generalized for a qudit system [33, 34]. Given an N-dimensional system that is described with n d-dimensional qudits, the QFT, $F(d,N)$, where $N = d^n$, transforms the computational basis

$$\{|0\rangle, |1\rangle, \ldots, |N-1\rangle\} \tag{23.4}$$

into a new basis set [35]

$$F(d,N)\,|j\rangle = \frac{1}{\sqrt{N}} \sum_{k=0}^{N-1} \mathrm{e}^{2\pi \mathrm{i} jk/N}\,|k\rangle \tag{23.5}$$

As a convention, an integer j is rephrased in a base-d form. If $j > 1$ then

$$j = j_1 j_2 \ldots j_n = j_1 d^{n-1} + j_2^{n-2} + \cdots + j_n d^0 \tag{23.6}$$

and, if $j < 1$, then

$$j = 0.j_1 j_2 \ldots j_n = j_1 d^{-1} + j_2 d^{-2} + \cdots + j_n d^{-n} \tag{23.7}$$

The QFT applied to a state $|j\rangle$ can be represented in a product form as

$$\begin{aligned}
|j\rangle = \left|j_1 j_2 \ldots j_n\right\rangle &\mapsto \frac{1}{d^{n/2}} \sum_{k=0}^{d^n-1} \mathrm{e}^{2\pi \mathrm{i} jk/d^n}\,|k\rangle \\
&= \frac{1}{d^{n/2}} \sum_{k_1=0}^{d-1} \cdots \sum_{k_n=0}^{d-1} \mathrm{e}^{2\pi \mathrm{i} j\left(\sum_{l=1}^{n} k_l d^{-l}\right)}\,|k_1 k_2 \ldots k_n\rangle \\
&= \frac{1}{d^{n/2}} \sum_{k_1=0}^{d-1} \cdots \sum_{k_n=0}^{d-1} \bigotimes_{l=1}^{n} \mathrm{e}^{2\pi \mathrm{i} jk_l d^{-l}}\,|k_l\rangle \\
&= \frac{1}{d^{n/2}} \bigotimes_{l=1}^{n} \left[\sum_{k_l=0}^{d-1} \mathrm{e}^{2\pi \mathrm{i} jk_l d^{-l}}\left|k_l\right\rangle\right]
\end{aligned}$$

The quantum circuit illustration of the process is shown in Figure 23.1, and the explicit expression of the product form is listed in Figure 23.1 on the right.

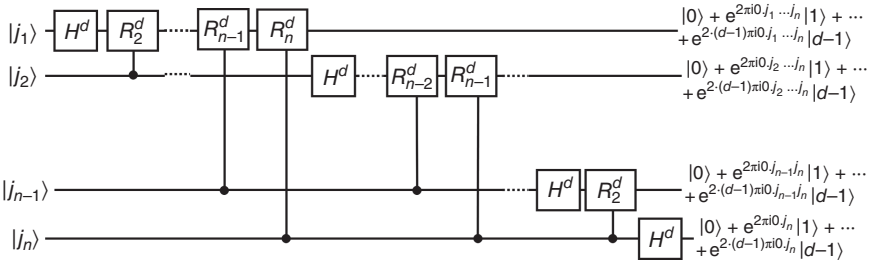

Figure 23.1 Circuit schematic of qudit quantum Fourier transform. The d-dimensional Hadamard gate is represented as H^d and the phase gate R^d is shown in Eq. (23.10). Explicit expressions of the qudit states are on the right. Source: Wang et al. [2], (figure 10) / Frontiers Media S.A / CC BY-4.0.

The generalized Hadamard gate H^d is equivalent to single qudit QFT as $H^d := F(d,d)$, which does the operation

$$H^d|j_n\rangle = |0\rangle + e^{2\pi i 0.j_n}|1\rangle + \cdots + e^{2(d-1)\pi i 0.j_n}|d-1\rangle \tag{23.8}$$

The matrix representation of H^d is

$$\begin{pmatrix} 1 & 1 & \cdots & 1 \\ 1 & e^{2\pi i 0.1} & \cdots & e^{2\pi i 0.(d-1)} \\ \vdots & \vdots & \ddots & \vdots \\ 1 & e^{2(d-1)\pi i 0.1} & \cdots & e^{2(d-1)\pi i 0.(d-1)} \end{pmatrix} \tag{23.9}$$

In the circuit the R_k^d gate is a phase gate that has the expression

$$R_k^d = \begin{pmatrix} 1 & 0 & \cdots & 0 \\ 0 & e^{2\pi i/d^k} & \cdots & 0 \\ \vdots & \vdots & \ddots & \vdots \\ 0 & 0 & \cdots & e^{2\pi i(d-1)/d^k} \end{pmatrix} \tag{23.10}$$

The black dots in the circuit are the MVCGs. The operation of which is applying R_k^d to the target qudit j times, when a control qudit is in state $|j\rangle$. In order to fix the sequence of $j_1 j_2 \ldots j_n$, a series of qudit SWAP gates are applied at the end, which are not explicitly drawn in Figure 23.1.

The qudit QFT provides a crucial subroutine for many qudits algorithms. Qudit QFT offers superior approximations where the error bound decreases exponentially with d [34], which outperforms its binary counterpart [36].

Once the qudit QFT is available, quantum PEA can be generalized to the qudit version [35]. The goal of qudit PEA is to obtain the phase on the eigenvalue of $|u\rangle$ under U, i.e. the phase factor r in $U|u\rangle = e^{2\pi i r}|u\rangle$. The PEA in the qudit system can be decomposed to two registers of qudits. The first register contains t qudits. To successfully obtain the phase factor r accurate to the s dits with a success probability of at least $1-\epsilon$, we choose t to be $t = s + \log_d(\frac{1}{2\epsilon} + 2)$ [35]. The assumption of performing an arbitrary number of times of the unitary operation U and the ability to initialize eigenvector $|u\rangle$ with the second register's qudits are similar to those of the qubit PEA [37].

As a convention, we rewrite the rational number r in a base-d form as

$$r = R/d^t = \sum_{l=1}^{t} \overline{R_l}/d^l = 0.\overline{R_1 R_2} \ldots \overline{R_t} \tag{23.11}$$

As shown in Figure 23.2a, we first apply the generalized Hadamard gates $H \equiv F(d,d)$ to each qudit in the first register. The following derivation of the explicit expressions of the PEA are summarized from Ref. [35]. The state of the lth qudit of the first register after the Hadamard gate is

$$F(d,d)\left|0_l\right\rangle = \frac{1}{\sqrt{d}} \sum_{k_l=0}^{d-1} \left|k_l\right\rangle \tag{23.12}$$

Then the lth qudit controls the operation $U^{d^{t-l}}$ applied on the target register qudits with the state $|u\rangle$. The controlled gate gives

$$CU^{d^{l-1}}|k\rangle \otimes |u\rangle = |k\rangle (U^{d^{t-l}})^k |u\rangle = e^{2\pi i k d^{t-l} r}|k\rangle \otimes |u\rangle \tag{23.13}$$

Notice that the controlled gate here is a MVCG such that the phase $e^{2\pi i k d^{t-l} r}$ is applied to $|u\rangle$ according to the state number k of the controlled qudit.

After all the controlled operations the resulting qudit system states become

$$\left(\prod_{l=1}^{t} \otimes \frac{1}{\sqrt{d}} \sum_{k_l=0}^{d-1} e^{2\pi i k_l d^{t-l} r} |k_l\rangle\right) \otimes |u\rangle \tag{23.14}$$

Then through a process called the "phase kick-back," the phase factor generated in the second register is passed on to the state of the first register such that

$$|\text{Register } 1\rangle = \frac{1}{d^{t/2}} \sum_{k=0}^{d^t-1} e^{2\pi i r k} |k\rangle \tag{23.15}$$

We can get the approximated eigenvalue r from the state number R of $|R\rangle$ by applying the inverse QFT to the qudits in the first register:

$$F^{-1}(d, d^t) |\text{Register } 1\rangle = |R\rangle \tag{23.16}$$

The full process of PEA is shown in Figure 23.2b.

Introducing qudits to the PEA not only reduces the number requirement of qudits and qudit gates but also decreases the error rate exponentially as the qudit dimension increases [38]. The qudit PEA enables the qudit variations of a long

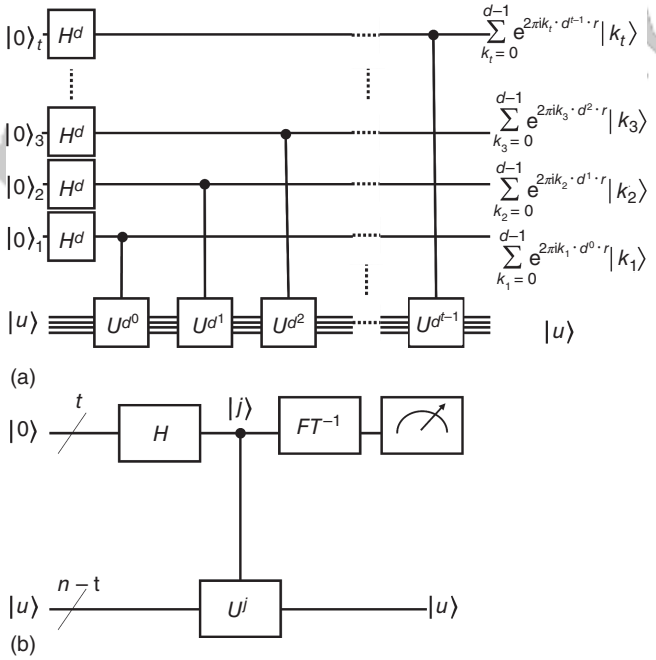

Figure 23.2 (a) First half of the PEA where the "phase kick-back" happens. The explicit states of the first register qudits after the U^j operations are giving on the right. (b) The simplified circuit of the PEA. After the Hadamard gate and controlled-U^j operations, the inverse Fourier Transform (FT^{-1}) is performed and the phase factor is obtained by measuring the first register qudits states. Source: Wang et al. [2], (figure 11) / Frontiers Media S.A / CC BY-4.0.

list of applications that includes Shor's factorization algorithm [39], simulation of quantum systems [40], quantum algorithm for solving linear equations [41, 42], and quantum counting [43]. Recently, a quantum algorithm solving a linear system using the qutrit version of the PEA has been proposed [44]. The qudit PEA has the potential to out-perform its qubit counterpart in those applications.

23.2 Qudit Implementation on Photonic Systems

Photonic system provides a good platform for quantum computing because photons have a comparatively long decoherence time. It is also a good candidate for qudit quantum computing since many of the physical properties of the photon, such as the orbital angular momentum [45, 46], frequency-bin [47–50] and time-bin [51, 52], have more than two states. There are examples of photonic qudit quantum computing such as the experimental realization of arbitrary multidimensional multiphotonic transformations [53] and experimental entanglement of high-dimensional qudits [47]. In Section 23.2.1, we review a photonic qudit computation scheme that makes use of the time and frequency degrees of freedom (DoF). To make connection between the reviewed photonic system to practical physical chemistry problems, we introduce an algorithm for open quantum dynamics in the last part of Section 23.2.1. In Section 23.2.2 we discuss the bosonic qudit in microwave cavity and its application in simulating the molecular vibration modes, an inherently multidimensional system.

23.2.1 Qudits in Time and Frequency Degrees of Freedom

In this section, we review a single photon system that integrated on-chip modulators, pulse shapers and other well-established fiber-optic components. This system can achieve the high-dimensional($d > 2$) high-fidelity Fourier-transform pulse shaping [48], acquire the two-qudit SUM gate via the time and frequency DoF [50] as well as demonstrate a proof-of-principle qutrit PEA [31].

First, we review a parallelizable scalable photonic frequency-bin manipulation platform [48]. It can realize qudit quantum computing based on electro-optic phase modulation and pulse shaping. The qudit in this scheme is represented by a single photon spread over d narrow-band modes with frequency centered at $\omega_n = \omega_0 + n\Delta\omega$ [54]. The operations applying on the qudit are implemented via a frequency multiport V connecting the input $\hat{a}_n^{(\mathrm{in})}$ and output $\hat{a}_m^{(\mathrm{out})}$ in a way $\hat{a}_m^{(\mathrm{out})} = \sum_n V_{mn}\hat{a}_n^{(\mathrm{in})}$ so the photon is manipulated in the desired fashion. The first crucial component to develop a fully functional qudit quantum circuit for the qudit PEA is the discrete QFT. QFT is equivalent to the high-dimensional Hadamard gate in the single qudit case. This step is realized with a balanced frequency tritter, the three-mode extension of the electro-optic-base frequency beam splitter. The single qutrit QFT achieved is in the form:

$$U = \frac{1}{\sqrt{3}}\begin{pmatrix} 1 & 1 & 1 \\ 1 & \mathrm{e}^{2\pi \mathrm{i}/3} & \mathrm{e}^{4\pi \mathrm{i}/3} \\ 1 & \mathrm{e}^{4\pi \mathrm{i}/3} & \mathrm{e}^{2\pi \mathrm{i}/3} \end{pmatrix} \tag{23.17}$$

Color Fig: **23.3**

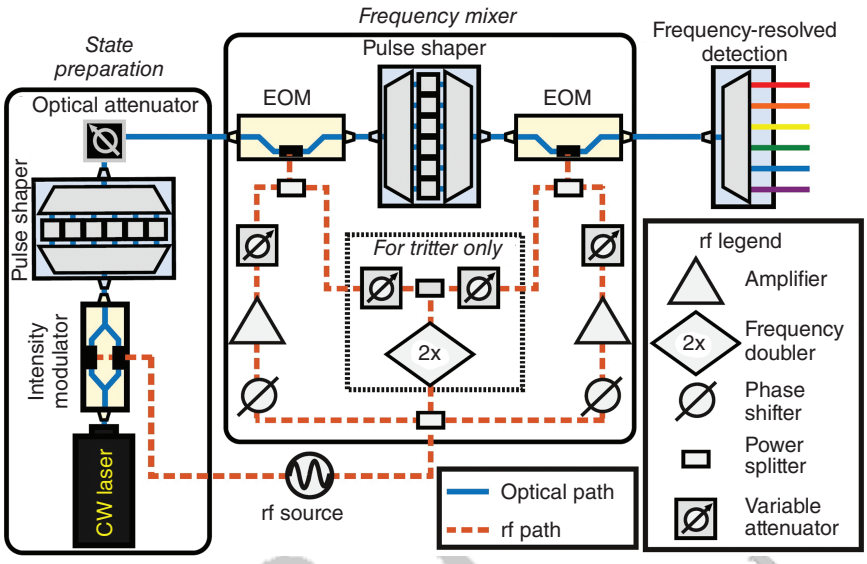

Figure 23.3 The experimental setup for the frequency beam splitter. Source: Reprinted from Lu et al. "Electro-optic frequency beam splitters and tritters for high-fidelity photonic quantum information processing." Physical review letters 120.3 (2018): 030502. Lu et al. [48] with the permission of American Physical Society under license RNP/22/FEB/050615.

The frequency beam splitter (whose schematic illustration is given in Figure 23.3) has three stages: State preparation, frequency mixer (build by a pulse shaper [PS] sandwiched between two electro-optic phase modulator [EOM]) and frequency-resolved detection. A radio-frequency (rf) oscillator provides a 25-GHz drive signal to each EOM. Combining with amplifiers and delay lines, it sets the amplitude and phase properly for each waveform. The central pulse shaper is used to implement the spectral phase pattern, which is optimized numerically, in order to perform the Hadamard gate. The frequency tritter is attained by incorporating an additional harmonic in the microwave drive signal with a rf frequency doubler as shown in the setup. The pulse shaper in the middle of two EOMs imparts the spectral phase that makes sure all the sidebands generated by the first EOM are reabsorbed to the computational space after the second one. This can circumvent the unavoidable scattering of the input photon causing by the EOM and assure the fully deterministic nature of the proposed frequency beam splitter[54]. This first ever demonstrated balanced frequency tritter acquires a fidelity as high as (0.9989 ± 0.0004) and provides the important building block toward scalable, high-fidelity qudit quantum computing based on frequency encoding [48].

The second crucial component of the qudit PEA is the two-qudit gate. With standard linear optics and photon counting, the interacting of the two photons is not deterministic and has probabilistic results [55], adding the difficulty to build a reliable controlled gate for the photonic qudits. The proposed photonic system bypasses this difficulty by encoding the qudits to two DoFs on a single photon – i.e. the time-bin and frequency-bin [50]. In this multidimensional time-bin and

frequency-bin settings, the distance of the frequency spacing (Δf) and the time-bin spacing (Δt) are chosen to surpass the Fourier Transform limit (i.e. $\Delta f \Delta t > 1$) so that the two DoFs can be manipulated independently in a hyper-encoding fashion [56, 57]. This is to ensure that each time-frequency mode pair establishes a well-defined entity that all the neighboring mode is separated sufficiently to achieve a reliable encoding. As discussed in Section 23.1.1, the qudit universal gate set requires the two-qudit gate as well as single qudit gate like X and Z gate. The Z gate can be accomplished with a phase modulator and a pulse shaper in the time domain and frequency domain, respectively. The frequency qudit X gate can be built with a Z gate sandwiched between two high-dimensional QFT gates [48]. The time-bin X gate can be done by the process of state-dependent delay. In a three-dimensional case for example, the time-bin $|0\rangle_t$ is separated from $|1\rangle_t$ and $|2\rangle_t$, and its route is delayed by three bins. The spatial separation is done by a Mach–Zehnder modulator (MZM) switch, and the illustration is shown in Figure 23.4. The gate output is measured by a single-photon detector (SPD) and a time interval analyzer. For the two-qudit gates shown in Figure 23.5, the control qudit is represented by the frequency DoF and the time DoF is the target qudit. The true single photon (instead of weak coherent states) used for the two-qudit gate is obtained from a frequency-bin entangled pair generated via spontaneous four-wave

Color Fig: **23.4**

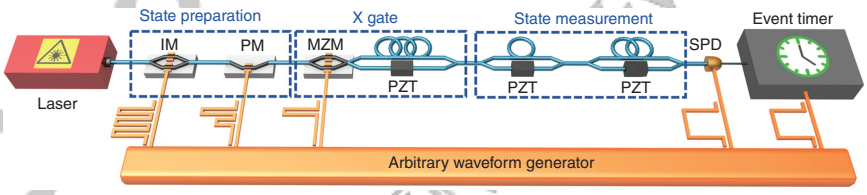

Figure 23.4 The full setup for the time-bin X gate. The components in the experiment are phase modulator (PM), intensity modulator (IM), piezo-electric-phase shifter (PZT), Mach–Zehnder modulator (MZM), and single-photon detector (SPD). The time-bin delay is indicated by the circle-shaped fibers. Source: Imany et al. [50], (figure 2a) / Springer Nature / CC BY-4.0.

Color Fig: **23.5**

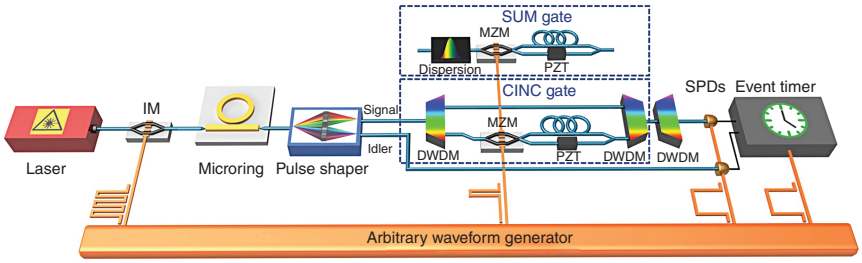

Figure 23.5 The illustration of the CINC and SUM gate experimental setup. In the CINC gate, the time bin $|2\rangle_t$ is separated from time bins $|0\rangle_t$ and $|1\rangle_t$ by the MZM. For the SUM gate, the outside time bins $|3\rangle_t$ and $|4\rangle_t$ are separated from the time bins $|0\rangle_t$, $|1\rangle_t$, and $|2\rangle_t$ inside the computational space by the MZM. The dense wavelength-division multiplexer is DWDM. Source: Imany et al. [50], (figure 3a) / Springer Nature / CC BY-4.0.

mixing in an on-chip silicon nitride microresonator. The time-bins are characterized by intensity modulation of the pump and couple into a microring resonator (with free spectral range $\Delta f = 380$ GHz and resonance line widths $\delta f \simeq 250$ MHz) to generate a biphoton frequency comb. The signal and idler photons from the first three comb-line pairs are selected out with a commercial pulse shaper. While the idler photons are sent to a SPD for heralding, the signal photons with the time and frequency qudits can be prepared to any product state $|m\rangle_t|n\rangle_f$ $(m, n = 0,1,2)$ and provide a full computational basis set.

The two types of two-qudit gates are the controlled increment (CINC) operation and the more complex SUM gate – a generalized controlled-NOT gate [58]. The CINC gate applies the X gate to time-bin qudit only when the frequency qudit is in the state $|2\rangle_f$. The CINC gate is implemented by separating $|2\rangle_f$ with a dense wavelength-division multiplexing (DWDM) filter, routing it to a time-bin X gate, and keeping other two frequency-bins unchanged. Another DWDM is used to bring back the frequency-bins with zero relative delay. The SUM gate adds the value of the control qudit to the value of the target qudit, modulo 3. It applies a cyclic shift of 1 slot delay to the time-bins associated with $|1\rangle_f$ and 2 slots delay to the time-bins corresponding to $|2\rangle_f$ and keeps those related to $|0\rangle_f$ unchanged. To employ the frequency-dependent delay to the time-bins, a chirped fiber Bragg grating (CFBG) is used to induce a dispersion of -2 ns/nm to the photon. The delay operations are linear and not cyclic and thus move some of the time-bins outside of the computational space. These time-bins can be returned to the computational space using principles identical to the time-bin X gate with a relative delay. In order to measure the transformation matrix of these gates in the computational basis, all nine combinations of single time-bins and frequency-bins are prepared with an intensity modulator (IM) and a pulse shaper as the input states. The signal counts in all possible output time-bin/frequency-bin pairs are recorded with the three different setups of DWDMs in the path of the signal photons to identify the different frequency-bins. The measured transformation matrix for the CINC gate has a so-called "classical" fidelity of $\mathcal{F}_C = 0.90 \pm 0.01$ and for the SUM gate the fidelity is $\mathcal{F}_C = 0.92 \pm 0.01$ [50, 59]. This fully deterministic photonic two-qudit gate setup can be integrated with on-chip components in a low cost, room temperature, and scalable manner. It lays down a foundation for building the qudit universal gate set and the high-dimensional quantum circuit in an integrated on-chip photonic platform.

Lastly, with the single qutrit QFT and two-qudit gate in hand, we review a demonstration of a proof-of-principle qutrit PEA [31]. Following the setup of the previous paragraph, the frequency DoF carries the control qutrit, and the time DoF carries the target qutrit. Some of the well-established techniques and fiber-optic components are used to assemble the quantum circuit including: phase modulator (PM), intensity modulator (IM), continuous-wave (CW) laser source, pulse shaper (PS), and chirped fiber Bragg grating (CFBG). The qutrit operations, as illustrated in Figure 23.6, are performed in three stages [31]: (i) a state preparation stage where the frequency-bin and time-bin of the input photon are initialized by a PM followed by a PS and an IM; (ii) a controlled-unitary operation stage where the MVCG gate (as described in

Color Fig: **23.6**

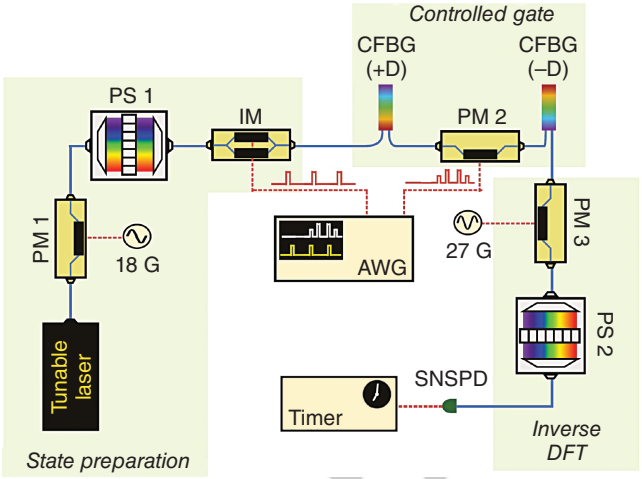

Figure 23.6 Experimental setup. Component (abbreviate) is, correspondingly, Fourier-transform pulse shaper (PS); Electro-optic phase/intensity modulator (PM/IM); Chirped fiber Bragg grating (CFBG); Arbitrary waveform generator (AWG); Superconducting nanowire single-photon detector (SNSPD). The AWG has a 10 MHz reference clock that is synchronized to both radio-frequency oscillators (18 and 27 GHz).) Source: Lu et al. [31]/John Wiley & Sons.

Section 23.1.1) is built with a PM sandwiched by two CFBGs; and (iii) an inverse Fourier Transformation and measuring stage where the phase information of the photon is extracted by a superconducting nanowire single-photon detector (SNSPD) connected to a timer. The inverse QFT comprises a PM and a PS. It is worth noting that the MVCG gate in the circuit applies different operations to the target qutrit based on the three unique states of the control qutrit. In the experiment, frequency and time-bin qutrits are sent through the control and target registers, respectively. In the measuring stage, the state of the control register qutrits is measured, and state distribution is recorded to obtain the phase information. The eigenphases obtained by this photonic PEA setup can be retrieved with 98% fidelity [31].

In Table 23.1 we provide results generated by the photonic PEA experiment. To demonstrate the ability of implementing qutrit PEA with the simplest unitary operation possible, the first experiment encoding the unitary operation as follow:

$$\hat{U}_1 = \mathrm{diag}(1, \omega, \omega^2) \tag{23.18}$$

with ω being the cubic root of unity. Then to utilize the repetition advantage of the photonic setup, i.e. the experiment can repeat the same setup at a relatively low cost, another more complex unitary is encoded in the circuit as:

$$\hat{U}_2 = \mathrm{diag}\left(1, \mathrm{e}^{\mathrm{i}0.351\pi}, \mathrm{e}^{\mathrm{i}1.045\pi}\right) \tag{23.19}$$

After a given number of experimental shots, we can obtain the statistical inference of the phase based on the numerical data. To do this, the statistical relation between the photon state distribution and eigenphase can be summarized as follows: given a eigenphase ϕ corresponding to one of the eigenstate, the probability of measuring

Table 23.1 Normalized photon counts and comparison of the true phase ϕ and the experimentally estimated phase ϕ' for each eigenstate of $\hat{U}_1$ (Eq. 23.18) and $\hat{U}_2$ (Eq. 23.19).

	$\hat{U}_1$		
Eigenstate	$\|0\rangle_t$	$\|1\rangle_t$	$\|2\rangle_t$
E_0	0.9948 ± 0.0004	0.0101 ± 0.0004	0.0122 ± 0.0005
E_1	0.0023 ± 0.0002	0.9805 ± 0.0009	0.0120 ± 0.0005
E_2	0.0029 ± 0.0002	0.0094 ± 0.0004	0.9758 ± 0.0010
True phase, ϕ	0	$2\pi/3$	$4\pi/3$
Est. phase, $\tilde{\phi}$	1.972π	0.612π	1.394π
Error, $\frac{\lvert\phi-\tilde{\phi}\rvert}{2\pi}$	1.4%	2.7%	3.0%
	$\hat{U}_2$		
Eigenstate	$\|0\rangle_t$	$\|1\rangle_t$	$\|2\rangle_t$
E_0	0.878 ± 0.002	0.316 ± 0.003	0.143 ± 0.002
E_1	0.032 ± 0.001	0.530 ± 0.003	0.318 ± 0.003
E_2	0.090 ± 0.002	0.154 ± 0.002	0.539 ± 0.003
True phase, ϕ	0	0.3511π	1.045π
Est. phase, $\tilde{\phi}$	1.859π	0.377π	1.045π
Error, $\frac{\lvert\phi-\tilde{\phi}\rvert}{2\pi}$	7.1%	1.3%	0.0%

Source: Ref. [31]/John Wiley & Sons.

the output state into $|n\rangle$, where $n \in \{0,1,2\}$, is

$$C(n,\phi) = \frac{1}{9}\left|1 + e^{i(\phi - \frac{n2\pi}{3})} + e^{i2(\phi - \frac{n2\pi}{3})}\right|^2 \tag{23.20}$$

Define E_0, E_1, and E_2 to be the probability of detecting the photons that fell into $|0\rangle_f$, $|1\rangle_f$, and $|2\rangle_f$. The estimated phase, denoted $\tilde{\phi}$, is the phase that has the smallest mean-square error between the measured and theoretical results:

$$\min_{\tilde{\phi}} \sum_{n=0}^{2} (E_n - C(n,\tilde{\phi}))^2 \tag{23.21}$$

The estimated phases for $\hat{U}_1$ (23.18) and $\hat{U}_2$ (23.19) are shown in Table 23.1 [31]. Although in the second experiment (with U_2) the eigenphases are chosen to be arbitrary values (not a fraction of π), they are derivable from the statistical distributions of the photon counts.

In many subjects of physical sciences such as physical chemistry, chemical physics, and materials science, the physical system of interest is often interacting with a larger environment whose scale and complexity prevent exact treatment by the time-dependent Schrodinger equation. To this end, the theory of open quantum dynamics uses a variety of approximations to average out the effects of environments and focus on the core system [60]. Recently, the open quantum dynamics formalism has been adapted to a quantum algorithm that can simulate

excitonic dynamics on molecular systems [61, 62]. As the quantum algorithm for open quantum dynamics relies on projection measurements on the output states to extract physical information, it is a natural candidate for implementation with the electro-optical system just described. Suppose the density matrix of the initial physical system can be described by a sum of different pure quantum states multiplied by the corresponding probabilities:

$$\rho = \sum_i p_i |\phi_i\rangle\langle\phi_i| \tag{23.22}$$

where each p_i denotes the probability of detecting each $|\phi_i\rangle$ in the mixed state of ρ. The dynamics is represented via the *Kraus operators* M_k in an operator sum representation [61]:

$$\rho(t) = \sum_k M_k \rho M_k^\dagger \tag{23.23}$$

Then each $|\phi_i\rangle$ can be prepared as an input state vector v_i of a given basis and evolved as follows:

$$|\phi_{ik}(t)\rangle = M_k v_i \xrightarrow{\text{unitary dilation}} U_{M_k}(v_i^T, 0, \ldots, 0)^T \tag{23.24}$$

In Eq. (23.24), the M_k is undergoing the 1-dilation process to become $U_{M_k} = \begin{pmatrix} M_k & D_{M_k^\dagger} \\ D_{M_k} & -M_k^\dagger \end{pmatrix}$ [61, 63], where $D_{M_k} = \sqrt{I - M_k^\dagger M_k}$ is the defect operator of M_k.

After the time evolution of $|\phi_{ik}(t)\rangle$, the population of each basis state can be retrieved by calculating the diagonal vector:

$$\text{diag}(\rho(t)) = \sum_{ik} p_i \cdot \text{diag}(|\phi_{ik}\rangle\langle\phi_{ik}|) \tag{23.25}$$

The $\text{diag}(|\phi_{ik}(t)\rangle\langle\phi_{ik}(t)|)$ is efficiently obtainable via the projection measurements on the first half subspace of $U_{M_k}(v_i^T, 0, \ldots, 0)^T$. This algorithm also supports the calculation of the expectation value of an observable $\langle A\rangle = \text{Tr}(A\rho(t))$. To ensure the contraction and positive-semidefinite requirement, we consider the operator $\tilde{A} = \frac{A + \mathbf{I}||A||}{2||A||}$ with the Cholesky decomposition $\tilde{A} = LL^\dagger$ [64]. Then the evolution of the observable is

$$L^\dagger|\phi_{ik}(t)\rangle = L^\dagger M_k v_i \xrightarrow{\text{unitary dilation}} U_{L^\dagger} U_{M_k}(v_i^T, \ldots, 0)^T \tag{23.26}$$

and $\langle\tilde{A}\rangle$ can be calculated by:

$$\langle\tilde{A}\rangle = \text{Tr}(\tilde{A}\rho(t)) = \sum_{i,k} \text{Tr}(p_i \cdot L^\dagger|\phi_{ik}(t)\rangle\langle\phi_{ik}(t)|L) \tag{23.27}$$

The trace of $L^\dagger|\phi_{ik}(t)\rangle\langle\phi_{ik}(t)|L$ is obtainable by applying the projection measurements into the first N-dimensional space of $U_{L^\dagger} U_{M_k}(v_i^T, 0, \ldots, 0)^T$ [61]. $\langle A\rangle$ can then be derived from $\langle\tilde{A}\rangle$ by $\langle A\rangle = 2||A||\langle\tilde{A}\rangle - ||A||$. In the algorithm, the projection operations facilitate the measurements of both the density matrix and the observable. Hu et al. [61] proposed and demonstrated this general quantum algorithm to evolve open quantum dynamics on quantum computing devices. Within the algorithm, Kraus operators are converted into unitary matrices with

minimal dilation guaranteed by the Sz.-Nagy theorem [63]. The algorithm is demonstrated on an amplitude damping channel using the IBM Qiskit quantum simulator and the IBM Q 5 Tenerife quantum device [61]. This general algorithm does not require particular models of dynamics or decomposition of the quantum channel and thus can be easily generalized to other open quantum dynamical models. Since projection operations can be performed naturally and efficiently on the electro-optical system, the open quantum dynamics algorithm is compatible and viable for implementation on this platform.

23.2.2 Superconducting Bosonic Processor

In this section, we review a photonic system that consists of microwave cavities and transmon qubits to implement a two-mode superconducting bosonic processor that enables the scalable simulation of molecular vibronic spectra [65]. The microwave cavity with its underlying bosonic structure provides a natural bosonic platform to simulate the inherently high-dimensional molecular vibrational modes. Although the read-out apparatus consists of a transmon qubit, the microwave cavity as the central component is simulating a multidimensional system and can be treated as a qudit in general.

The simulation of molecular vibronic spectra is to study the electronic transition accompanied with the vibrational dynamics. Keeping the adiabatic Born–Oppenheimer approximation that separates the nuclear and electronic DoF, each of the distinct electronic states forms a potential-energy surface (PES) that carries a unique manifold of vibrational eigenstate. The normal modes of the electronic vibration can be acquired with a harmonic approximation: keeping only the quadratic terms of the displacement of the PES about the equilibrium. The corresponding transformation of the set of creation and annihilation operators $\hat{\mathbf{a}} = (\hat{a}_1, \dots, \hat{a}_N)$ for N vibrational modes can be described with the Duschinsky transformation [66]. The Duschinsky transformation can be disintegrated into Gaussian operations in terms of the Doktorov operator [67]

$$\hat{\mathbf{a}} \to \hat{U}_{\text{Dok}} \hat{\mathbf{a}} \hat{U}_{\text{Dok}}^{\dagger}, \quad \hat{U}_{\text{Dok}} = \hat{\mathbf{D}}(\boldsymbol{\alpha}) \hat{\mathbf{S}}^{\dagger}(\boldsymbol{\zeta}') \hat{\mathbf{R}}(U) \hat{\mathbf{S}}(\boldsymbol{\zeta}) \tag{23.28}$$

where

$$\hat{\mathbf{D}}(\boldsymbol{\alpha}) = \hat{D}(\alpha_1) \otimes \hat{D}(\alpha_1) \otimes \cdots \otimes \hat{D}(\alpha_N) \tag{23.29}$$

$$\hat{\mathbf{S}}^{\dagger}(\boldsymbol{\zeta}') = \hat{S}^{\dagger}(\zeta_1') \otimes \hat{S}^{\dagger}(\zeta_2') \otimes \cdots \otimes \hat{S}^{\dagger}(\zeta_N') \tag{23.30}$$

$\hat{\mathbf{D}}(\boldsymbol{\alpha})$ and $\hat{\mathbf{S}}(\boldsymbol{\zeta})$ describe a tensor product of single-mode displacement and squeezing operations across all N modes correspondingly. $\hat{\mathbf{R}}(U)$, the N-mode rotation operator, is represented by an $N \times N$ rotation matrix U which can be generated with a product of two-mode beam splitter operations [10]. The set of dimensionless Doktorov parameters $\boldsymbol{\alpha} = (\alpha_1 \dots \alpha_N)$, $\boldsymbol{\zeta} = (\zeta_1 \dots \zeta_N)$, $\boldsymbol{\zeta}' = (\zeta_1' \dots \zeta_N')$ can be derived from molecular structural information in the different electronic configurations. In the $N = 2$ case , U has the form of a two-dimensional rotation matrix with a single free parameter, i.e. the angle θ. The transitions between the vibrational states due to a

Color Fig: **23.7**

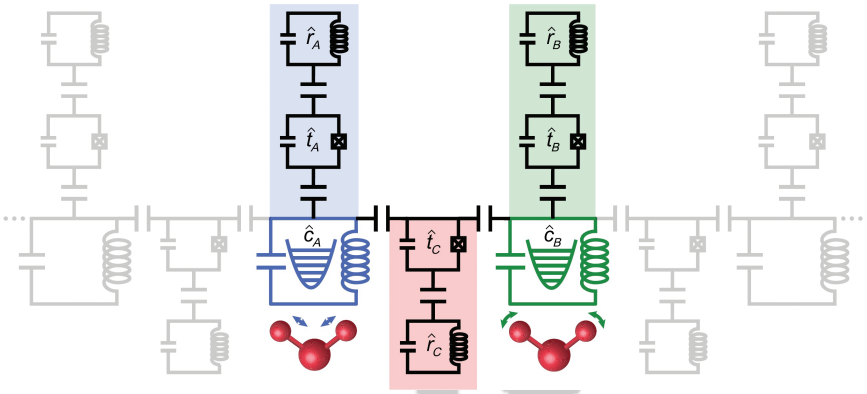

Figure 23.7 The superconducting bosonic processor circuit. Two microwave cavity modes are denoted in blue $\hat{c}_A$, and green $\hat{c}_B$. Ancilla measurement and control modules consist of a transmon qubits ($\hat{t}_A, \hat{t}_B$) and readout resonators ($\hat{r}_A, \hat{r}_B$) coupled to each cavity mode have blue and green shades correspondingly. The transmon qubit serving as the coupler module $\hat{t}_C$ and readout resonator $\hat{r}_C$ is shaded red. To illustrate the scalability of this configuration, a linear array of N cavity modes (with N ancillary modules) connected by coupler modules with its nearest-neighbor have light gray shades. Source: Wang et al. [65], (figure 1) / American Physical Society / CC BY-4.0.

sudden change in electronic PES is emulated as applying $\hat{U}_{\text{Dok}}$ to an initial state $|\psi_0\rangle$ of the bosonic processor. This projection produces the Franck–Condon factors (FCFs) which are the vibrational overlap integrals of an initial pretransition vibrational eigenstate, $|\hat{n}\rangle$ with a final post-transition vibrational eigenstate, $\left|\hat{n}'\right\rangle$:

$$\text{FCF}|_{\hat{n},\hat{n}'} = |\left\langle \hat{n}' \right| \hat{U}_{\text{Dok}} |\hat{n}\rangle|^2 \tag{23.31}$$

The FCFs have practical importance that can provide insights of the structure and dynamic nature of the excited electronic states.

The superconducting bosonic processor (as shown in Figure 23.7) is designed to employ the bosonic modes of two microwave cavities $\hat{c}_A$ and $\hat{c}_B$. The two cavities are dispersively coupled by a coupler transmon $\hat{t}_C$ which facilitates the beam splitter and squeezing operations through driven four-wave mixing processes [68]. A readout resonator $\hat{r}_C$ is dispersively connected to the coupler transmon. The cavity modes displacement is operated via resonant drives through local coupling ports. Two ancillary transmon-readout systems $\hat{t}_A, \hat{r}_A$ and $\hat{t}_B, \hat{r}_B$ are added to the device and coupled to each cavity to execute state preparation and tomography. The photonic state of the quantum processor is used to simulate the transformation of a molecular vibrational state caused by the electronic transition. In the state initialization process, both bosonic modes are prepared in vacuum state via feedback cooling protocols and initialized to the Fock state $|n, m\rangle$ using optimal control techniques [69]. This bosonic processor has the ability to synthesize arbitrary Fock states reliably allowing the simulation of FCFs starting from vibrationally excited states which outperforms most other bosonic simulators. The Doktorov transformation is then implemented by triggering a basis change to that of the post-transition

vibrational Hamiltonian. In the $N = 2$ case, a single beam splitter is used to apply the rotation operation. The four-wave mixing capabilities of the coupler transmon help enforce the single-mode squeezing and beam splitter operations. Two pump tones (with frequencies $\omega_{1/2}$) couple to the coupler transmon through a port to matching the appropriate frequency condition such that $\omega_1 + \omega_2 = 2\omega_{A/B}$ for the squeezing operation and $\omega_2 - \omega_1 = \omega_B - \omega_A$ where $\omega_{A/B}$ are the cavity frequencies. This realizes the desired Hamiltonians [68]

$$\hat{H}_{\mathrm{BS}}/\hbar = g_{\mathrm{BS}}(t)(\mathrm{e}^{\mathrm{i}\varphi}\hat{c}_A\hat{c}_B^\dagger + \mathrm{e}^{-\mathrm{i}\varphi}\hat{c}_A^\dagger\hat{c}_B) \tag{23.32}$$

$$\hat{H}_{\mathrm{sq},i}/\hbar = g_{\mathrm{sq},i}(t)(\mathrm{e}^{\mathrm{i}\phi_i}\hat{c}_i^2 + \mathrm{e}^{-\mathrm{i}\phi_i}\hat{c}_i^{\dagger 2}) \tag{23.33}$$

where $\hat{c}$ denotes the creation operator of the microwave mode and $i \in \{A, B\}$, g_{BS} and $g_{\mathrm{sq},i}$ are the coupling coefficients for beam splitters and squeezing operations where the explicit form can be found in Ref. [68]. It is worth noticing that the phase factors of the Hamiltonians $\{\varphi, \phi_i\}$ are controlled by the phase of the pump tones that facilitate the performance of $\hat{U}_{\mathrm{Dok}}$ with the correct family of beam splitters and squeezing operations. A post-selecting process in terms of transmon measurement rejects the heating events of the transmons that can dephase the cavities and halt the pumped operations. This postselection also initializes the ancillas to their ground states for the subsequent measurement of the cavities. Finally, the desired FCFs are derived from the average photon numbers of the repeating cavities measurements.

There are two complementary measurement schemes for extracting FCFs from the final state. The shared basic idea of the two measurement schemes is to make use of the dispersive coupling of each microwave cavity to its ancillary transmon-readout system [65]:

$$\hat{H}_{\mathrm{int}}/\hbar = -\sum_{i\in\{A,B\}} \chi_i \hat{c}_i^\dagger \hat{c}_i \hat{t}_i^\dagger \hat{t}_i \tag{23.34}$$

where $\hat{H}_{\mathrm{int}}$ is the interaction Hamiltonian and $\hat{c}$ and $\hat{t}$ denote the creation operator of the microwave mode and transmon qubit respectively. The first scheme, single-bit extraction, uses the state-selective π pulses to build the mapping between a given joint cavity photon number population $\{n', m'\}$ and the joint state of the two transmons. The frequencies of the pulses are $\omega_{t_A} = \omega_{t_A}^0 - n'\chi_A + (n'^2 - n')(\chi_A'/2)$ and $\omega_{t_B} = \omega_{t_B}^0 - m'\chi_B + (m'^2 - m')(\chi_B'/2)$. In this case the small second-order dispersive shift is also taken into account:

$$\hat{H}'_{\mathrm{int}}/\hbar = \sum_{i\in\{A,B\}} (\chi_i'/2)\hat{c}_i^\dagger \hat{c}_i^\dagger \hat{c}_i \hat{c}_i \hat{t}_i^\dagger \hat{t}_i \tag{23.35}$$

Here in this experiment $\chi_A' = 2\pi \times 1.31$ kHz and $\chi_B' = 2\pi \times 1.35$ kHz [65]. The read-out of the individual transmons uses the standard dispersive techniques, and the results are obtained in a shot-by-shot basis where a single bit of information is extracted from each joint photon number state been probed. Notice that this single-bit extraction of FCFs is not scalable as the bosonic Hilbert space grows exponentially with the number of modes N. To overcome the scalability issue, the second measurement scheme implements single-shot photon number resolving detection. Based on the dispersive Hamiltonian between the cavity mode and transmon ancilla, a quantum nondemolition (QND) mapping of arbitrary binary

valued operator of the cavity Hilbert space to the state of transmon can be achieved by driving the transmon with numerically optimized waveforms $\epsilon(t)$ [69, 70],

$$\hat{H}_{\text{drive}}/\hbar = \epsilon^*(t)\hat{t} + \epsilon(t)\hat{t}^\dagger \tag{23.36}$$

Here QND means the measurement process preserves the physical integrity of the measured system [71]. Therefore, the number of photons for a given cavity state can be measured in the binary form $|n\rangle = |\prod_{k=0}^{k_{\max}} b_k\rangle$, where $n = \prod_{k=0}^{k_{\max}} 2^{b_k}$ and $\{b_k\} \in \{0,1\}$ and $k_{\max}$ is the number of binary digits in n. Each bit b_k can be measured sequentially in a given run of the experiment. The QND nature of each measuring operations allows the sequential application of the mapping pulses to the cavity states followed by transmon measurements. These mappings project an initial cavity state $|\psi\rangle = \sum c_n|n\rangle$ with n up to 16 into a definite Fock state $|n\rangle$ with the probability $|c_n|^2$. The advantage of the photon number resolved sampling protocol compared to the single-bit extraction is a notable reduction of the simulator runs required within a desired statistical error on all output probabilities.

The FCFs of a given electronic transition can be used to derive the relative intensities of the progressions in photo-electron vibronic spectra. The simulated FCFs are under the harmonic approximation and may deviate from the measured actual molecular spectra due to the vibrational anharmonicity in the true PES. In order to show the simulator's capability of large photon numbers generation and measurement, we review the simulation of the FCFs of water molecule (as shown in Figure 23.8) as an example of a long vibronic progressions simulation [65]. The water molecule starting in the vacuum state ($|\psi_0\rangle = |n,m\rangle \;\; n = 0, m = 0$) transforms under photoionization to the second excited state ($\tilde{B}^2B_2$) of doublet spin multiplicity, and there is B_2 symmetry to the attendant electronic wave function. The process can be described as

$$H_2O \xrightarrow{h\nu} H_2O + (\tilde{B}^2B_2) + e^- \tag{23.37}$$

Color Fig: **23.8**

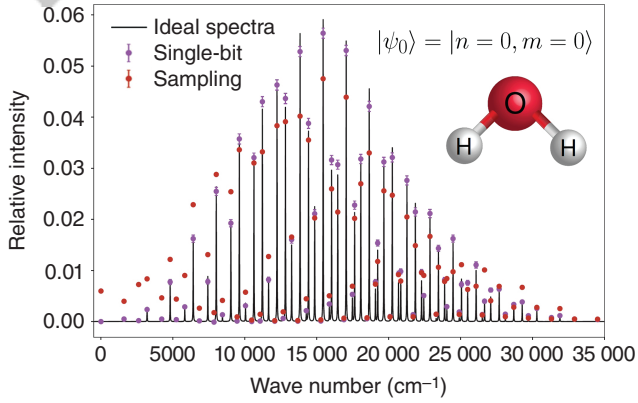

Figure 23.8 Franck–Condon factors for the photoionization of the water molecule. The theoretical FCFs, artificially broadened with Lorentzian profiles (10 cm^{-1} FWHM), is depicted by the solid lines. Purple and red circles represent experimental data using the single-bit extraction and sampling measurement scheme, respectively. Source: Wang et al. [65], (figure 3a) / American Physical Society / CC BY-4.0.

To quantify the quality of the quantum simulation, we introduce the distance $D = \frac{1}{2}\sum_{i=0}^{n_{\max}}\sum_{j=0}^{n_{\max}}|p_{ij}^{\text{meas}} - p_{ij}^{\text{ideal}}|$ between the measured probabilities p_{ij}^{meas} and the ideal distribution p_{ij}^{ideal}. The distance for the water molecule simulation is 0.049. Another relevant metric is run time. In the experiment with repetition rate of roughly 300 Hz, the data acquisition run time of 3×10^4 samples of the photoionization of water with single bit extraction and photon number resolved sampling is 7 hours vs. 100 seconds, respectively. Furthermore, because of the postselection of transmon heating events, all the metrics are accompanied with a success probability of 95%. Other detailed simulation data of the experiment could be found in the supplementary materials of Ref. [65].

The bosonic system has an inherent advantage in simulating the transformation of a bosonic Hamiltonian compared to the conventional qubit processor. It can encode the vibrational dynamics of the system naturally and decompose the Doktorov transformation into Gaussian operations efficiently. A recent proposal of obtaining FCFs on a spin-1/2 quantum computer requires $n_g = O[N^2 n_{\max}^2 \log^3(1/\epsilon)]$ gates to implement $\hat{U}_{\text{Dok}}$ with a universal qubit gate set within an error of ϵ [72]. The choice of $n_{\max}$ depends on the initial state as well as the magnitude of the displacement and squeezing. As a comparison, this native N modes bosonic simulator only requires $2N$ squeezing operations, N displacement operations, and a maximum of $N(N-1)/2$ nearest-neighbor beam splitter operations [73]. This equivalent to a total of $O[N^2]$ operations and a corresponding circuit depth of $O[N]$ when non-overlapping beam splitters are applied simultaneously [65]. To sum up, the superconducting bosonic processor has the potential to integrate all of the necessary components of qudit quantum computing to implement high-fidelity, scalable, and resource-efficient simulation of molecular vibronic spectra and outperform its conventional qubit counterpart.

23.3 Summary and Future Outlooks

In quantum computing, qudit is an alternative computational unit that uses multiple states for information storage and processing. Photonic systems make natural platforms for qudit quantum computing given the multidimensional nature in many photon properties. This review chapter first introduces the basic ideas and methods of qudit quantum computing that include qudit gates, universality, and important qudit algorithms such as the QFT and the PEA. Next, it introduces two physical realizations of qudit computing with photonic systems. The first system is an electro-optic platform that integrates on-chip modulators, pulse shapers, and other well-established fiber-optic components to build all the crucial components for a proof-of-principle qutrit PEA. The second system is a two-mode superconducting bosonic processor consisting of microwave cavities and transmon qubits to simulate molecular vibronic spectra.

Compared to the conventional qubits, qudits can reduce circuit complexity, simplify experimental setup, and enhance quantum algorithm efficiency. For example, the number of gates required to build the universal qudit set under

Muthukrishnan and Stroud's proposal achieves a $(\log_2 d)^2$ scaling advantage compared to that of the qubits [12, 32]. This number is reduced by another factor of n (the number of qudits) in Luo and Wang's proposed scheme [13]. The MVCG gate (as shown in Section 23.1.1) can reduce the circuit depth by lowering the number of controlled gates. The electro-optic photonic platform is the first physical system that has been demonstrated to perform the MVCG gate, which compressed multiple control operations in a single shot. The two-qudits-out-of-one-photon scheme makes sure the controlled-gate is deterministic and increases the fidelity of the setup. All the fiber-optic components in this scheme can be integrated on-chip making it compact and scalable. Furthermore, this platform can process and measure thousands of photons simultaneously, which enables the fast generation of statistical patterns: this feature enables the electro-optic platform to realize a proposed statistical phase estimation that loses the prior knowledge requirement of the eigenstates and thus offers more flexibility in searching eigenphase-eigenstate pairs within some specified range of interest [74]. As for the bosonic processor discussed in Section 23.2.2, it is shown that simulating a multidimensional system with a qudit-like system such as the microwave cavity can reduce the operation requirement by a large amount. The single-shot photon number resolving detection scheme can resolve the photon numbers with a notable reduction of the simulator runs. This bosonic processor is expandable by coupling more cavities where each of them is combined with ancilla measurement and control modules. The scalability of the system grants it the potential to simulate more complicated many-boy complex systems [75].

Acknowledgments

We acknowledge the financial support of National Science Foundation under award number 2124511, CCI Phase I: NSF Center for Quantum Dynamics on Modular Quantum Devices (CQD-MQD), and Award No. 2124511-CHE, NSF 1839191-ECCS.

References

1 Brylinski, J.-L. and Brylinski, R. (2002). Universal quantum gates. In: *Mathematics of quantum computation*, (ed. R.K. Brylinski, G. Chen) 117–134. Chapman and Hall/CRC.
2 Wang, Y., Hu, Z., Sanders, B.C., and Kais, S. (2020). Qudits and high-dimensional quantum computing. *Frontiers in Physics* 8: 479.
3 Vlasov, A.Y. (2002). Noncommutative tori and universal sets of nonbinary quantum gates. *Journal of Mathematical Physics* 43 (6): 2959–2964.
4 Gottesman, D. (1999). Fault-tolerant Quantum computation with higher-dimensional systems. In: *Quantum Computing and Quantum Communications*, vol. 1509 (ed. C.P. Williams) *NASA International Conference on Quantum Computing and Quantum Communications*, 302–313. Berlin: Springer-Verlag.

5 Daboul, J., Wang, X., and Sanders, B.C. (2003). Quantum gates on hybrid qudits. *Journal of Physics A: Mathematical and General* 36: 2525–2536.

6 Zhou, D.L., Zeng, B., Xu, Z., and Sun, C.P. (2003). Quantum computation based on *d*-level cluster state. *Physical Review A* 68: 062303.

7 Bullock, S.S., O'Leary, D.P., and Brennen, G.K. (2005). Asymptotically optimal quantum circuits for *d*-level systems. *Physical Review Letters* 94: 230502.

8 Li, W.-D., Gu, Y.-J., Liu, K. et al. (2013). Efficient universal quantum computation with auxiliary Hilbert space. *Physical Review A* 88: 034303.

9 Mischuck, B. and Mølmer, K. (2013). Qudit quantum computation in the Jaynes-Cummings model. *Physical Review A* 87: 022341.

10 Reck, M., Zeilinger, A., Bernstein, H.J., and Bertani, P. (1994). Experimental realization of any discrete unitary operator. *Physical Review Letters* 73: 58–61.

11 Rowe, D.J., Sanders, B.C., and de Guise, H. (1999). Representations of the Weyl group and Wigner functions for SU(3). *Journal of Mathematical Physics* 40 (7): 3604–3615.

12 Muthukrishnan, A. and Stroud, C.R. (2000). Multivalued logic gates for quantum computation. *Physical Review A* 62: 052309.

13 Luo, M. and Wang, X. (2014). Universal quantum computation with qudits. *Science China Physics, Mechanics & Astronomy* 57: 1712–1717.

14 Brennen, G.K., O'Leary, D.P., and Bullock, S.S. (2005). Criteria for exact qudit universality. *Physical Review A* 71: 052318.

15 Patera, J. and Zassenhaus, H. (1988). The Pauli matrices in n dimensions and finest gradings of simple lie algebras of type A_{n-1}. *Journal of Mathematical Physics* 29 (3): 665–673.

16 Gottesman, D., Kitaev, A., and Preskill, J. (2001). Encoding a qubit in an oscillator. *Physical Review A* 64 (1): 012310.

17 Bartlett, S.D., de Guise, H., and Sanders, B.C. (2002). Quantum encodings in spin systems and harmonic oscillators. *Physical Review A* 65: 052316.

18 Nielsen, M.A., Bremner, M.J., Dodd, J.L. et al. (2002). Universal simulation of Hamiltonian dynamics for quantum systems with finite-dimensional state spaces. *Physical Review A* 66: 022317.

19 Howard, M. and Vala, J. (2012). Qudit versions of the qubit $\pi/8$ gate. *Physical Review A* 86: 022316.

20 Wilmott, C.M. (2011). On swapping the states of two qudits. *International Journal of Quantum Information* 09 (06): 1511–1517.

21 Wilmott, C.M. and Wild, P.R. (2012). On a generalized quantum swap gate. *International Journal of Quantum Information* 10 (03): 1250034.

22 Mermin, N.D. (2001). From classical state swapping to quantum teleportation. *Physical Review A* 65: 012320.

23 Fujii, K. (2003). Exchange gate on the qudit space and Fock space. *Journal of Optics B: Quantum and Semiclassical Optics* 5: S613–S618.

24 Paz-Silva, G.A., Rebić, S., Twamley, J., and Duty, T. (2009). Perfect mirror transport protocol with higher dimensional quantum chains. *Physical Review Letters* 102: 020503.

25 Wang, X. (2001). Continuous-variable and hybrid quantum gates. *Journal of Physics A: Mathematical and General* 34: 9577–9584.

26 Alber, G., Delgado, A., Gisin, N., and Jex, I. (2001). Efficient bipartite quantum state purification in arbitrary dimensional Hilbert spaces. *Journal of Physics A: Mathematical and General* 34: 8821–8833.

27 Garcia-Escartin, J.C. and Chamorro-Posada, P. (2013). A swap gate for qudits. *Quantum Information Processing* 12: 3625–3631.

28 Ralph, T.C., Resch, K.J., and Gilchrist, A. (2007). Efficient Toffoli gates using qudits. *Physical Review A* 75: 022313.

29 Kiktenko, E.O., Nikolaeva, A.S., Xu, P. et al. (2020). Scalable quantum computing with qudits on a graph. *Physical Review A* 101: 022304.

30 Di, Y.-M. and Wei, H.-R. (2013). Synthesis of multivalued quantum logic circuits by elementary gates. *Physical Review A* 87: 012325.

31 Lu, H.-H., Hu, Z., Alshaykh, M.S. et al. (2019). Quantum phase estimation with time-frequency qudits in a single photon. *Advanced Quantum Technologies* 0 (0): 1900074.

32 Nielsen, M.A. and Chuang, I.L. (2011). *Quantum Computation and Quantum Information: 10th Anniversary Edition*, 10e. New York: Cambridge University Press.

33 Stroud, A.M.C.R. (2002). Quantum fast Fourier transform using multilevel atoms. *Journal of Modern Optics* 49 (13): 2115–2127.

34 Zilic, Z. and Radecka, K. (2007). Scaling and better approximating quantum Fourier transform by higher radices. *IEEE Transactions on Computers* 56: 202–207.

35 Cao, Y., Peng, S.-G., Zheng, C., and Long, G.-L. (2011). Quantum Fourier transform and phase estimation in qudit system. *Communications in Theoretical Physics* 55: 790–794.

36 Coppersmith, D. (2002). An approximate Fourier transform useful in quantum factoring. *arXiv preprint quant-ph/0201067*.

37 Bocharov, A., Roetteler, M., and Svore, K.M. (2017). Factoring with qutrits: Shor's algorithm on ternary and metaplectic quantum architectures. *Physical Review A* 96: 012306.

38 Parasa, V. and Perkowski, M. (2011). Quantum phase estimation using multivalued logic. *2011 41st IEEE International Symposium on Multiple-Valued Logic*, pp. 224–229, May 2011.

39 Shor, P.W. (1994). Algorithms for quantum computation: discrete logarithms and factoring. *Proceedings 35th Annual Symposium on Foundations of Computer Science*, pp. 124–134, November 1994.

40 Abrams, D.S. and Lloyd, S. (1999). Quantum algorithm providing exponential speed increase for finding eigenvalues and eigenvectors. *Physical Review Letters* 83: 5162–5165.

41 Harrow, A.W., Hassidim, A., and Lloyd, S. (2009). Quantum algorithm for linear systems of equations. *Physical Review Letters* 103: 150502.

42 Pan, J., Cao, Y., Yao, X. et al. (2014). Experimental realization of quantum algorithm for solving linear systems of equations. *Physical Review A* 89 (2): 022313.

43 Tonchev, H.S. and Vitanov, N.V. (2016). Quantum phase estimation and quantum counting with qudits. *Physical Review A* 94: 042307.

44 Sawerwain, M. and Leoński, W. (2013). Quantum circuits based on qutrits as a tool for solving systems of linear equations. *arXiv:1309.0800*.

45 Babazadeh, A., Erhard, M., Wang, F. et al. (2017). High-dimensional single-photon quantum gates: concepts and experiments. *Physical Review Letters* 119: 180510.

46 Erhard, M., Fickler, R., Krenn, M., and Zeilinger, A. (2018). Twisted photons: new quantum perspectives in high dimensions. *Light: Science & Applications* 7: 17146.

47 Kues, M., Reimer, C., Roztocki, P. et al. (2017). On-chip generation of high-dimensional entangled quantum states and their coherent control. *Nature* 546 (6760): 622–626.

48 Lu, H.-H., Lukens, J.M., Peters, N.A. et al. (2018). Electro-optic frequency beam splitters and tritters for high-fidelity photonic quantum inf. process. *Physical Review Letters* 120 (3): 030502.

49 Imany, P., Jaramillo-Villegas, J.A., Odele, O.D. et al. (2018). 50-GHz-spaced comb of high-dimensional frequency-bin entangled photons from an on-chip silicon nitride microresonator. *Optics Express* 26 (2): 1825–1840.

50 Imany, P., Jaramillo-Villegas, J.A., Alshaykh, M.S. et al. (2019). High-dimensional optical quantum logic in large operational spaces. *npj Quantum Information* 5: 59.

51 Islam, N.T., Lim, C.C.W., Cahall, C. et al. (2017). Provably secure and high-rate quantum key distribution with time-bin qudits. *Science Advances* 3 (11): e1701491.

52 Humphreys, P.C., Metcalf, B.J., Spring, J.B. et al. (2013). Linear optical quantum computing in a single spatial mode. *Physical Review Letters* 111: 150501.

53 Gao, X., Erhard, M., Zeilinger, A., and Krenn, M. (2020). Computer-inspired concept for high-dimensional multipartite quantum gates. *Physical Review Letters* 125: 050501.

54 Lukens, J.M. and Lougovski, P. (2017). Frequency-encoded photonic qubits for scalable quantum information processing. *Optica* 4: 8–16.

55 Knill, E., Laflamme, R., and Milburn, G.J. (2001). A scheme for efficient quantum computation with linear optics. *Nature* 409 (6816): 46–52.

56 Fang, W.-T., Li, Y.-H., Zhou, Z.-Y. et al. (2018). On-chip generation of time-and wavelength-division multiplexed multiple time-bin entanglement. *Optics Express* 26 (10): 12912–12921.

57 Humphreys, P.C., Kolthammer, W.S., Nunn, J. et al. (2014). Continuous-variable quantum computing in optical time-frequency modes using quantum memories. *Physical Review Letters* 113 (13): 130502.

58 Wang, X., Sanders, B.C., and Berry, D.W. (2003). Entangling power and operator entanglement in qudit systems. *Physical Review A* 67: 042323.

59 De Greve, K., McMahon, P.L., Yu, L. et al. (2013). Complete tomography of a high-fidelity solid-state entangled spin–photon qubit pair. *Nature Communications* 4 (1): 1–7.

60 Breuer, H.-P. and Petruccione, F. (2002). *The Theory of Open Quantum Systems*. Oxford University Press on Demand.

61 Hu, Z., Xia, R., and Kais, S. (2020). A quantum algorithm for evolving open quantum dynamics on quantum computing devices. *Scientific Reports* 10 (1): 1–9.

62 Hu, Z., Head-Marsden, K., Mazziotti, D.A. et al. (2021). A general quantum algorithm for open quantum dynamics demonstrated with the Fenna-Matthews-Olson complex. *arXiv preprint arXiv:2101.05287*.

63 Levy, E. and Shalit, O.M. (2014). Dilation theory in finite dimensions: the possible, the impossible and the unknown. *Rocky Mountain Journal of Mathematics* 44 (1): 203–221.

64 Krishnamoorthy, A. and Menon, D. (2013). Matrix inversion using Cholesky decomposition. *2013 Signal Processing: Algorithms, Architectures, Arrangements, and Applications (SPA)*, pp. 70–72, IEEE.

65 Wang, C.S., Curtis, J.C., Lester, B.J. et al. (2020). Efficient multiphoton sampling of molecular vibronic spectra on a superconducting bosonic processor. *Physical Review X* 10: 021060.

66 Duschinsky, F. (1937). The importance of the electron spectrum in multi atomic molecules. Concerning the Franck-Condon principle. *Acta Physicochimica URSS* 7: 551–566.

67 Doktorov, E., Malkin, I., and Man'Ko, V. (1977). Dynamical symmetry of vibronic transitions in polyatomic molecules and the Franck-Condon principle. *Journal of Molecular Spectroscopy* 64 (2): 302–326.

68 Gao, Y.Y., Lester, B.J., Zhang, Y. et al. (2018). Programmable interference between two microwave quantum memories. *Physical Review X* 8: 021073.

69 Heeres, R.W., Reinhold, P., Ofek, N. et al. (2017). Implementing a universal gate set on a logical qubit encoded in an oscillator. *Nature Communications* 8 (1): 1–7.

70 Krastanov, S., Albert, V.V., Shen, C. et al. (2015). Universal control of an oscillator with dispersive coupling to a qubit. *Physical Review A* 92: 040303.

71 Johnson, B., Reed, M., Houck, A.A. et al. (2010). Quantum non-demolition detection of single microwave photons in a circuit. *Nature Physics* 6 (9): 663–667.

72 Sawaya, N.P. and Huh, J. (2019). Quantum algorithm for calculating molecular vibronic spectra. *The Journal of Physical Chemistry Letters* 10 (13): 3586–3591.

73 Low, G.H. and Chuang, I.L. (2017). Optimal Hamiltonian simulation by quantum signal processing. *Physical Review Letters* 118 (1): 010501.

74 Moore, A.J., Wang, Y., Hu, Z. et al. (2021). Statistical approach to quantum phase estimation. *New Journal of Physics* 23: 113027.

75 Kais, S., Whaley, K., Dinner, A., and Rice, S. (2014). Quantum information and computation for chemistry. In: *Advances in Chemical Physics*, ed. S.A. Rice, A.R. Dinner). Wiley.

"keywords/abstract

Dear Author,

Keywords and abstracts will normally not be included in the print version of your chapter but only in the online version (if not decided differently by Wiley-VCH).

Thank you!"

Abstract

In quantum computing, qudit is a multilevel computational unit. Qudit, as an alternative to qubit, has a larger state space for information storage and processing. Quantum circuit built with qudits can enhance algorithm efficiency, reduce the circuit complexity, and simplify the experiment. Photonic systems with their comparatively long decoherence time provide good platforms for quantum computing. Some photonic systems also provide suitable working platforms for qudit quantum computing because qudit systems can be encoded naturally and conveniently with photons given the multidimensional nature in many photon properties. This chapter first introduces the basic knowledge and concepts of qudit quantum computing that include qudit gates, universality, and important qudit algorithms such as the quantum Fourier transform and the Phase Estimation Algorithm (PEA). It then reviews two implementations of qudit computing with photonic systems. The first system is an electro-optic platform that integrates on-chip modulators, pulse shapers, and other well-established fiber-optic components. This platform is capable of performing high-fidelity quantum Fourier transform pulse shaping and the two-qudit SUM gate via the time and frequency degrees of freedom, which paves the way to demonstrate a proof-of-principle qutrit PEA. The second system consists of microwave cavities and transmon qubits to implement a two-mode superconducting bosonic processor that enables the scalable simulation of molecular vibronic spectra.

Keywords

quantum information; quantum computing; qudit space; quantum phase estimation algorithm; electro-optic platform; superconducting bosonic processor and open quantum dynamics